Published in final edited form as:

Proc IEEE Int Symp Biomed Imaging. 2015 April ; 2015: 1443–1446. doi:10.1109/ISBI.2015.7164148.

UNSUPERVISED SHAPE PRIOR MODELING FOR CELL SEGMENTATION IN NEUROENDOCRINE TUMOR

Fuyong Xing[*,†] and **Lin Yang**[†]

[*]Department of Electrical and Computer Engineering, University of Florida

[†]J. Crayton Pruitt Family Department of Biomedical Engineering, University of Florida

Abstract

Automated and accurate cell segmentation provides support for many quantitative analyses on digitized neuroendocrine tumor (NET) images. It is a challenging task due to complex variations of cell characteristics. In this paper, we incorporate unsupervised shape priors into an efficient repulsive deformable model for automated cell segmentation on NET images. Unlike other supervised learning based shape models, which usually require a large number of annotated data for training, the proposed algorithm is an unsupervised approach that applies group similarity to shape constraints to avoid any labor intensive annotation. The algorithm is extensively tested on 51 NET images, and the comparative experiments with the state of the arts demonstrate the superior performance of this method using an unsupervised shape model.

Index Terms

Cell segmentation; NET; unsupervised shape prior

1. INTRODUCTION

Neuroendocrine tumor (NET) is one of the most frequent cancers worldwide. Computer-aided image analysis, like Ki67 counting, of digitized specimens could potentially support improved characterization of NET. Efficient and accurate cell segmentation is a prerequisite for many computer-aided quantitative analyses such as morphological feature extraction or cell recognition, which is critical for Ki-67 counting. Many state-of-the-art approaches such as multiple level set [1], supervised learning [2], and semi-supervised classification [3] have been successfully applied to nuclei/cell segmentation on microscopic images.

Cells on NET images usually exhibit missing, weak, or misleading boundaries (see Figure 1). Together with inhomogeneous intensity, these factors present significant challenges for many cell segmentation approaches. In order to address these limitations, a principle component analysis (PCA)-based shape prior has been presented in [4] to constrain the segmented contours with training data. Cai *et al.* [5] have applied shape constraints to a gradient vector flow model, while a shape prior-based level set method is reported in [6]. Recently, sparse representation [7, 8] has been proposed for shape prior modeling in biomedical image segmentation.

However, the aforementioned shape prior models require a large set of annotated data for training, which are often unavailable or labor intensive. Meanwhile, we also need to make an assumption that existing training shapes are sufficient to model new shapes in the testing data, which might not hold in many situations. Recently, Zhou *et al.* [9] have used the group similarity of object shapes in multiple images to assist the cardiac segmentation for ultrasound images. Inspired by this idea, we introduce unsupervised shape priors into a local deformable model for NET cell segmentation. The proposed approach is significantly different from Zhou's model [9] in several aspects. First, we do not need to assume the landmark correspondence among multiple shapes to be a priori, and instead they can be automatically and dynamically calculated during shape deformation; second, we exploit a sparse manifold learning method to build multiple subpopulation shape priors, which can deal with large shape variations on cells; finally, the proposed method can efficiently handle multiple touching or overlapping cells with shape preserving. The proposed cell segmentation algorithm can effectively handle weak or misleading cell boundaries, and provide significant support for subsequent cellular feature extraction and quantification in computer-aided diagnosis.

2. METHODS

In the proposed automated cell segmentation framework, we first employ a voting-based seed detection algorithm [10] to localize cell centers on each image and initialize contours (shapes) based on these detected centers, one per cell. Next, we calculate the landmark correspondence among different shapes and perform the proposed repulsive deformable model with locality and group similarity constraints.

2.1. Unsupervised Shape Prior Model

In this paper, cell shape is represented by the concatenated 2D coordinates of landmarks on the shape. Due to complex NET image nature, it is difficult to obtain accurate initial cell shapes for landmark correspondence establishing. Therefore, we propose to automatically and dynamically calculate the landmark correspondence during contour deformation. Since cells in NET images usually appear as approximate ellipses, we can compute the correspondences based on estimated major axes of cell shapes. Given the detected cell centers $\{(sx_i, sy_i)\}_{i=1}^{N}$, a set of N circles with centers $\{(sx_i, sy_i)\}$ are generated and the initial landmarks are evenly sampled along the circles. During contour evolution, the landmarks can be detected by the rules: 1) The two endpoints of the major axis of the contour are selected as major landmarks. 2) All the other landmarks are evenly sampled from the contour.

For cell shapes with established landmark correspondence, we assume that there exists a certain affine transform between any two shapes considering the fact that cell shapes are approximately elliptical. In this case, the shape matrix, which corresponds to a set of cells on one image, is a low-rank matrix, whose rank measures the correlation among shapes. A lower rank indicates smaller variation on cell shapes. Therefore, we propose to use the rank of shape matrix to measure the group similarity, which captures the global changes (translation, rotation, and scaling) of cell shapes [9].

Considering an image with N cells, we have N shapes $\{c_i=[x_1^i \ldots x_p^i\, y_1^i \ldots y_p^i]^T \in R^{2p\times 1}\}_{i=1}^N$ with each consisting of p landmarks. Shapes c_i and c_j follow $[x_k^i\, y_k^i]^T = A_i[x_k^j\, y_k^j]^T + T_i$, where $[x_k^i\, y_k^i]$ (or $[x_k^j\, y_k^j]$) is the k-th landmark on c_i (or c_j), and $A_i = [a_{11}^i\, a_{12}^i; a_{21}^i\, a_{22}^i] \in R^{2\times 2}$ together with $T_i = [t_1^i\, t_2^i]^T \in R^{2\times 1}$ denotes an affine transformation. Without losing generality, we assume that c_i, $i \neq 1$ is created from c_1 though affine transformation z_i:

$$c_i = S z_i,\ z_i = [\, a_{11}^i \ \ a_{12}^i \ \ a_{21}^i \ \ a_{22}^i \ \ t_1^i \ \ t_2^i \,]^T,\ \forall_i,$$
$$S = \begin{bmatrix} x^1 & y^1 & 0 & 0 & 1 & 0 \\ 0 & 0 & x^1 & y^1 & 0 & 1 \end{bmatrix}, \quad (1)$$

where $x^1 \in R^{p\times 1}$ and $y^1 \in R^{p\times 1}$ are the first and second half of c_1. Therefore, we have $X = [c_1\, c_2 \ldots c_N] = S[z_1\, z_2 \ldots z_N]$. Since the column space of $S \in R^{2p\times 6}$ has a dimensionality that is not larger than 6, the shape matrix X has low rank: rank(X) ≤ 6. The rank of X is then used to measure the degree of variations in cell shapes, and thus we can incorporate the low-rank constraint into shape deformation (discussed in Section 2.2) to truncate local variations but preserve global changes among different shapes. In this way, the model can effectively handle partially missing or misleading boundaries.

Due to shape variations of cells, it might be insufficient to learn a single shape prior model for all the shape instances. Therefore, we can build multiple subpopulation shape prior models based on clustered shapes. Furthermore, since the shape dimensionality is larger than the number of constraints of shape control, the shape vectors may lie on a low-dimensional manifold, where the similarly is measured by geodesic distance. Thus there exists a mapping Q transforming from the manifold to the original space

$$c_i = Q(v_i) + \varepsilon_i, \quad (2)$$

where $v_i \in R^{m\times 1}$ represents c_i in the embedding low-dimensional manifold and $\varepsilon_i \in R^{2p\times 1}$ denotes the noise. We use sparse manifold clustering and embedding (SMCE) [11] to obtain the low-dimensional embedding of the shape vectors. In cell segmentation, we have tested different dimensions (2, 3, 4, 5, and 6) as the dimensionality in the embedded low-dimensional manifold, and the variation is less than 1% with respect to the performance. We therefore chose a two-dimensional embedded manifold. Specifically, we first align all the shapes into a specified shape and cluster these aligned shapes into several groups with SMCE, and thereafter perform shape deformation with corresponding shape constraints independently within each individual group.

2.2. Local Repulsive Deformable Model

In this paper, we incorporate an unsupervised shape prior constraint into a local deformation model for cell segmentation. We choose the well-known Chan-Vese model [12] as the energy functional due to its robustness to image noise. In addition, we introduce an edge

detector into the model to further assist with separating cells from the background. Formally, for image I with N cells, the Chan-Vese model with an unsupervised shape prior constraint can be described as follows

$$\min_{X} \lambda_1 \sum_{i=1}^{N} \int_{\Omega_i} (I(\mathbf{x}) - h_i)^2 d\mathbf{x} + \lambda_2 \int_{\Omega_b} (I(\mathbf{x}) - h_b)^2 d\mathbf{x} + \lambda_3 \sum_{i=1}^{N} \int_0^1 e(c_i(s)) ds + \gamma \sum_{i=1}^{N} |c_i|, s.t. \operatorname{rank}(X) \leq K, \quad (3)$$

where Ω_i and Ω_b represent the regions inside c_i and outside all the contours, respectively, h_i (or h_b) denotes the average intensity of Ω_i (or Ω_b), $e(c_i(s))$ is the edge detector and chosen as $-\|\nabla I(c_i(s))\|^2$ ($s \in [0, 1]$ is the parameter for contour representation), $|c_i|$ denotes the length of c_i, and K is a predefined parameter controlling the rank of shape matrix X.

The model in (3) might not be able to separate touching/overlapping cells, and active contours may cross and merge one another during their evolution. To address this limitation, we introduce a repulsive term [10] into (3) to model the interaction between contours. Furthermore, because each cell is often surrounded by a limited number of adjacent cells, and only its neighboring cells make dominant repulsive contributions to its shape deformation during evolution. We thus can deform shape c_i in its local coordinate system to improve computational efficiency, and it is implemented by simply using c_i's M nearest neighbors C_i:

$$\min_{X} G(X) + \omega \sum_{i=1}^{N} \sum_{j \in C_i} \int_{\Omega_i \cap \Omega_j} 1 \, d\mathbf{x}, \; s.t. \; \operatorname{rank}(X) \leq K, \quad (4)$$

where $G(X)$ is equal to the objective function in (3). The repulsion in (4) reduces the computational complexity significantly from $\mathcal{O}\left(N^2\right)$ to $\mathcal{O}(N \cdot M)$ due to $M \ll N$, and optimizing (4) is faster than that using global repulsion without sacrificing segmentation accuracy.

2.3. Proximal Gradient

It is difficult to optimize (4) since rank is a discrete operator. Fortunately, we can achieve a relaxed form of (4) by replacing the rank operator with the nuclear norm $\|X\|_*$ [13, 9]:

$$\min_{X} G(X) \omega \sum_{i=1}^{N} \sum_{j \in C_i} \int_{\Omega_i \cap \Omega_j} 1 \, d\mathbf{x} + \eta \|X\|_*. \quad (5)$$

The energy function (first two terms) in (5) is differentiable with Lipschitz continuous gradient, so we exploit the proximal gradient method [14] to solve (5), which iteratively

updates current X based on its previous estimation and converges to a stationary point at a convergence rate of $\mathcal{O}\left(\frac{1}{k}\right)$

$$X^{k+1}=\arg\min_X \frac{1}{2}\|X-[X^k-\frac{1}{\mu}\nabla F\left(X^k\right)\|_F^2+\frac{\eta}{\mu}\|X\|_*, \quad (6)$$

where $F(X)=G(X)+\omega\sum_{i=1}^{N}\sum_{j\in C_i}\int\Omega_i\cap\Omega_j 1\, d\mathbf{x}$ and μ is a consonant. The gradient is defined as $\nabla F\left(X^k\right)=[\nabla f_1\left(c_1^k\right)\ldots\nabla f_N\left(c_N^k\right)]$ with $f_i(c_i)$ corresponding to the c_i's energy function, and $\nabla f_i(c_i(s))$ can be expressed as

$$\begin{aligned}\nabla f_i(c_i(s))=&(-\lambda_1(I(c_i(s))-h_i)^2+\lambda_2(I(c_i(s))-h_b)^2\\&-\lambda_3\nabla e(c_i(s))-\omega\sum_{j\in C_i}u_j(c_i(s))+\gamma\kappa(c_i(s)))\mathbf{n}_i(s),\end{aligned} \quad (7)$$

where $\mathbf{n}_i(s)$ and $\kappa(c_i(s))$ are the normal unit vector and curvature of c_i at landmark s, respectively, and $u_j(\mathbf{x})$ represents the indicator function: $u_j(\mathbf{x})=1$ if $\mathbf{x}\in\Omega_j$, otherwise 0. Given the initial contours, we can iteratively evolve the contours toward desired cell boundaries using (6).

3. RESULTS AND DISCUSSION

The proposed method has been extensively tested using 51 NET images with 1784 cells, which are captured at 40× magnification. The ground truth of cell contours are manually annotated for quantitative comparison. Each cell contour is represented by 60 landmarks, and the number of shape clusters is 2. In the experiments, we evaluate the model performance with respect to different ratios of η and μ in (6). We empirically set $\lambda_1=1$, $\lambda_2=1$, $\lambda_3=0.2$, $\gamma=1$, and $\omega=1.2$ in (7). Since one cell is usually surrounded by no more than 5 cells, we choose $M=5$ in (7).

We first perform qualitative analysis to evaluate the proposed method. Figure 2 presents the segmentation results using the proposed method on two sample slide digitized images, and hundreds of cells are accurately segmented with shape preserving. Figure 3 gives the comparative segmentation results on two representative image patches including mean shift (MS), isoperimetric (ISO) [15], superpixel (SUP) [16], marker-based watershed (MWS), graph-cut and coloring (GCC) [17], repulsive level set (RLS) [10], and the proposed method. It is clear that MS, ISO, and SUP are general segmentation algorithms which require further processing to obtain fair results. GCC suffers from inhomogeneous intensity. MWS and RLS provide more accurate results; however, they do not take advantage of the cellular shape constraints. On the contrary, the proposed approach can handle weak or misleading cell boundaries because of the shape prior constraint, and therefore provides best performance.

To quantitatively analyze the pixel-wise segmentation accuracy, we apply multiple metrics [9] including Dice similarity coefficient (*DSC*), Hausdorff distance (*HD*), and mean absolute distance (*MAD*), to the evaluation of the algorithm:

$$\begin{aligned} DSC &= \frac{2|\Omega_{sr} \cap \Omega_{gt}|}{|\Omega_{sr}| + |\Omega_{gt}|}, \\ HD &= \max\{\sup_s d\left(c_{sr}\left(s\right), c_{gt}\right), \sup_s d\left(c_{gt}\left(s\right), c_{sr}\right)\}, \\ MAD &= \frac{\int_0^1 d\left(c_{sr}\left(s\right), c_{gt}\right) \left|c'_{sr}\left(s\right)\right| ds}{2|c_{sr}|} \\ &\quad + \frac{\int_0^1 d\left(c_{gt}\left(s\right), c_{sr}\right) \left|c'_{gt}\left(s\right)\right| ds}{2|c_{gt}|} \end{aligned} \tag{8}$$

where Ω_{sr} and Ω_{gt} represent regions inside the automatic segmentation contour c_{sr} and the ground truth contour c_{gt}, respectively. $d(c_{sr}(s), c_{gt})$ denotes the minimum distance from point s at c_{sr} to the contour c_{gt}, *sup* means the supremum, and $|c_{sr}|$ represents the length of c_{sr}. Figure 4 displays the comparative performance between the proposed approach and the state of the arts. As one can tell, the proposed method provides the best accuracy, especially in terms of *HD* that calculates the largest error for each segmentation. This is attributed to the fact that compared with the other methods without shape constraints, the proposed approach can correct the corrupted cell boundaries and recover clean shapes. Meanwhile, the lower variations in the measurements indicate the stronger reliability of the proposed method.

The regularization parameter η in (6) plays an important role in segmentation. Table 1 shows the HD accuracy with respective to different η on 332 touching/overlapping cells, which usually exhibit weak or misleading boundaries. If η is too small (less than 5), the shape constraint is very weak such that some corrupted contours can not be recovered; however, if η is assigned a much higher value (larger than 20), it provides too strong penalty to the nuclear norm such that the final contours in each group will be more similar to each other. In the paper, $\eta = 20$ is chosen. It also demonstrates that contour evolution with shape prior is much better than the case without shape constraint ($\eta = 0$).

4. CONCLUSION

In this work, we incorporate an unsupervised shape prior constraint into a local repulsive active contour model. The landmark correspondence among different shapes is automatically determined during shape deformation and multiple subpopulation shape prior models based on sparse manifold learning are built to handle shape variations. The proposed algorithm does not require label intensive human annotations and meanwhile is effective and efficient for cell segmentation.

Acknowledgments

This research is funded, in part, by NIH 1R01AR065479-01A1.

References

1. Chang H, Han J, Spellman PT, Parvin B. Multireference level set for the characterization of nuclear morphology in glioblastoma multiforme. TBME. 2012; 59(12):3460–3467.

2. Kong H, Gurcan M, Belkacem-Boussaid K. Partitioning histopathological images: an integrated framework for supervised color-texture segmentation and cell splitting. TMI. 2011; 30(9):1661–1677.
3. Su H, Yin Z, Huh S, Kanade T. Cell segmentation in phase contrast microscopy images via semi-supervised classification over optics-related features. MedIA. 2013; 17(7):746–765.
4. Cootes TF, Taylor CJ, Cooper DH, Graham J. Active shape models-their training and application. CVIU. 1995; 61(1):38–59.
5. Cai H, Xu X, Lu J, Lichtman JW, Yung SP, Wong STC. Repulsive force based snake model to segment and track neuronal axons in 3d microscopy image stacks. NeuroImage. 2006; 32(4):1608–1620. [PubMed: 16861006]
6. Ali S, Madabhushi A. An integrated region-, boundary-, shape-based active contour for multiple object overlap resolution in histological imagery. TMI. 2012; 31(7):1448–1460.
7. Zhang S, Zhan Y, Metaxas DN. Deformable segmentation via sparse shape representation and dictionary learning. MIA. 2012; 16(7):1385–1396.
8. Xing F, Yang L. Robust selection-based sparse shape model for lung cancer image segmentation. MICCAI. 2013; 8151:404–412.
9. Zhou X, Huang X, Duncan JS, Yu W. Active contours with group similarity. CVPR. 2013:2969–2976.
10. Qi X, Xing F, Foran DJ, Yang L. Robust segmentation of overlapping cells in histopathology specimens using parallel seed detection and repulsive level set. TBME. 2012; 59(3):754–765.
11. Elhamifar E, Vidal R. Sparse manifold clustering and embedding. NIPS. 2011:55–63.
12. Chan TF, Vese LA. Active contours without edges. TIP. 2001; 10(2):266–277.
13. Cai J, Candes E, Shen Z. A singular value thresholding algorithm for matrix completion. SIAM J Optimization. 2010; 20(4):1956–1982.
14. Nesterov Y. Gradient methods for minimizing composite objective function. CORE Discussion Papers. 2007
15. Grady L, Schwartz EL. Isoperimetric graph partitioning for image segmetentation. TPAMI. 2006; 28(1):469–475.
16. Mori G. Guiding model search using segmentation. CVPR. 2005:1417–1423.
17. Al-Kofahi Y, Lassoued W, Lee W, Roysam B. Improved automatic detection and segmentation of cell nuclei in histopathology images. TBME. 2010; 57(4):841–852.

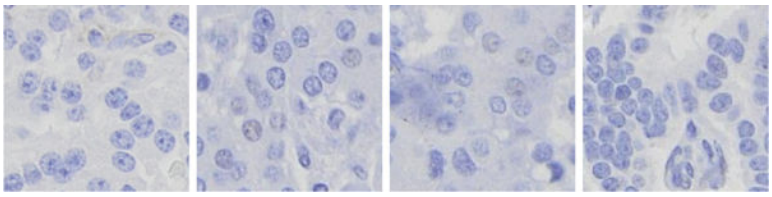

Fig. 1.
Several sample NET images. Many cells exhibit weak or misleading boundaries.

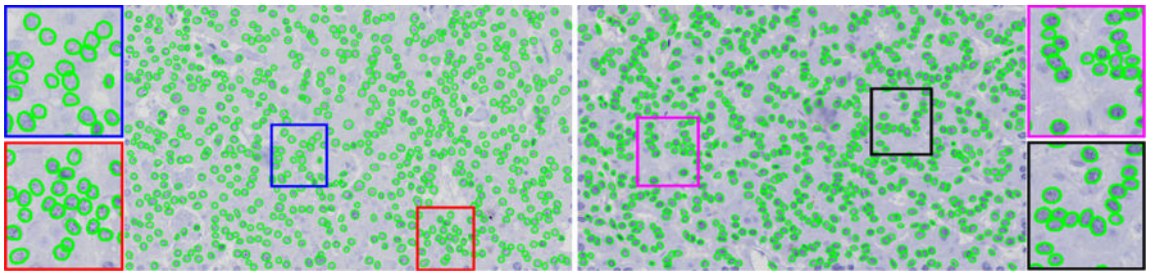

Fig. 2.
Segmentation results using the proposed algorithm on sample images (Cells touching image boundaries are ignored).

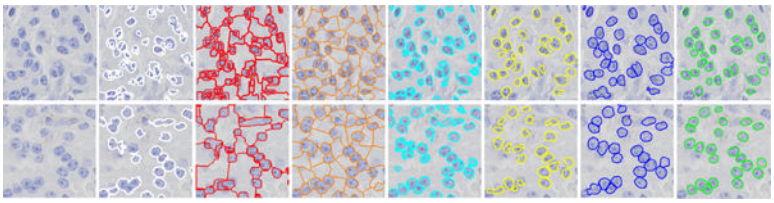

Fig. 3.

Comparative segmentation on two sample patches. From left to right: original images, MS, ISO [15], (SUP) [16], GCC [17], MWS, RLS [10], and the proposed method. MWS, RLS, and the proposed method use the same initialization.

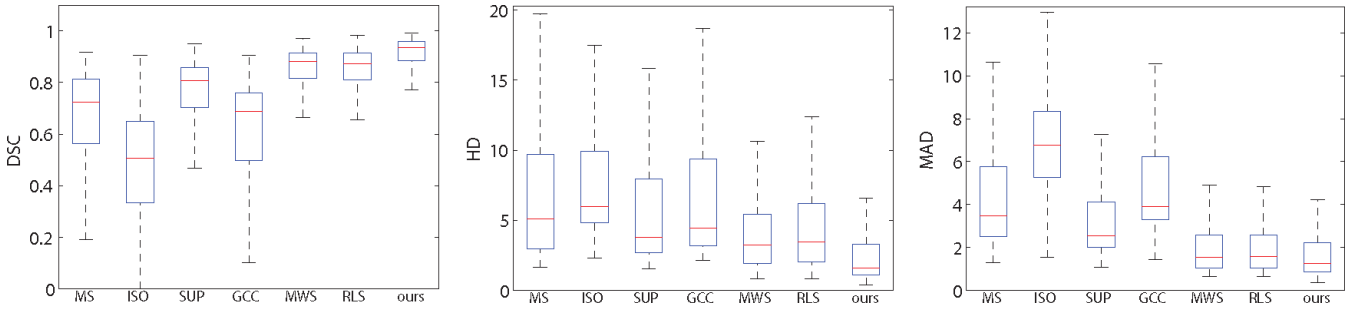

Fig. 4.

Box plot for quantitative comparison (DSC, HD, and MAD) between the proposed method (ours) and the other state of the arts.

Table 1

Comparative pixel-wise segmentation accuracy

η	Mean	Median	Standard Deviation	80%
0	6.16	5.06	4.34	9.79
1	6.04	4.85	4.33	9.63
5	5.64	4.34	4.25	9.24
10	5.32	3.88	4.08	9.03
20	4.97	3.74	3.69	8.10
60	5.40	4.51	3.01	7.39
100	6.60	6.09	2.92	8.28